Asociación Argentina
de Mecánica Computacional

Mecánica Computacional Vol XXXII, págs. 1183-1197 (artículo completo)
Carlos G. García Garino, Aníbal E. Mirasso, Mario A. Storti, Miguel E. Tornello (Eds.)
Mendoza, Argentina, 19-22 Noviembre 2013

SEISMIC SPECTRAL MONITORING OF CO_2 IN A GEOLOGICAL RESERVOIR

Julián L. Gómez and Claudia L. Ravazzoli

CONICET and Departamento de Geofísica Aplicada, Facultad de Ciencias Astronómicas y Geofísicas, Universidad Nacional de La Plata, Paseo del Bosque s/n, La Plata, Argentina,
jgomez@fcaglp.unlp.edu.ar, http://www.fcaglp.unlp.edu.ar/~jgomez

Keywords: Two-phase flow, spectral attributes, seismic reflectivity, CO_2

Abstract. Peak frequency is a spectral seismic attribute widely used for reservoir thickness estimation and hydrocarbon detection. In this work we apply this attribute in the context of the geological storage of carbon dioxide (CO_2) and analyze its reliability as a thickness estimator for the gas accumulation. To model the vertical distribution of CO_2, we solve the Buckley-Leverett equation with discontinuous flux function. A matrix reflectivity algorithm then computes, in the frequency domain, the seismic reflectivity. We find that the peak frequency variability due to CO_2 saturation does not alter significantly its correlation with the accumulation thickness. We then extend the applicability of the spectral attribute by examining its time-lapse response to the evolution of the injected CO_2 volume within a reservoir. We find that a description of the CO_2-brine contact as well as the evaluation of the reservoir's caprock sealing capacity can be obtained from this implementation. Peak-frequency time-lapse signatures when the CO_2 forms an up-going front, evolves into a growing accumulation and leaks into the caprock are identified.

1 INTRODUCTION

The geological storage of industrial carbon dioxide (CO_2) has the potential to provide a viable short-term mitigation of its atmospheric loading and subsequent green-house effect. In this context, the seismic characterization of the injected CO_2 in a reservoir is of prime importance for volume capacity evaluation and long-term site performance. The seismic spectral attribute *peak-frequency* or *tuning frequency* has been widely utilized for thickness estimation in conventional hydrocarbon reservoirs (Marfurt and Kirlin, 2001; Puryear and Castagna, 2008). Recently Williams and Chadwick (2012) have utilized the peak frequency with notable results to map thin CO_2 accumulations at the Sleipner CO_2 sequestration site.

The purpose of this study is to analyze the performance of the peak frequency for thickness estimation of a CO_2 accumulation and to test its potential as a time-lapse monitoring tool. We show that the peak frequency attribute is a robust indicator for CO_2 accumulation thickness. We find that its variability due to the CO_2 overall saturation does not alter significantly its correlation with layer thickness. We then extend the range of applicability of thepeak frequency and examine its changes in time as a tool for tracking the CO_2 flow and for leakage detection.

The CO_2 reservoir considered in this article is modeled after the Sleipner site at the North Sea, Norway. Since 1996, millions of tonnes of CO_2 have been injected at the Utsira formation, a large permeable high-porosity sandy aquifer located at a depth from 700 to 1000 m. The upward migration of the injected supercritical CO_2 due to buoyancy effects amounts to about 250 m and seems to have been stopped by the caprock situated at the top of the formation (Chadwick et al., 2005).

2 PEAK FREQUENCY AND LAYER THICKNESS

To derive the relationship between peak frequency and layer thickness we consider the analytical expression for the seismic reflectivity for an elastic and acoustic media due to a layer of thickness h between two halfspaces. The layer reflectivity is given by Liu and Schmitt (2003)

$$R_L(f,\theta_1) = \frac{i(Z_2^2 - Z_1 Z_3)\sin(k_{z2}h) + (Z_3 - Z_1)Z_2\cos(k_{z2}h)}{i(Z_2^2 + Z_1 Z_3)\sin(k_{z2}h) + (Z_3 + Z_1)Z_2\cos(k_{z2}h)}, \tag{1}$$

where $i = \sqrt{-1}$, f is the frequency and $k_{z2} = |k_2|\cos\theta_2$, the vertical component of the wavenumber vector, of modulus $|k_2|$. $Z_j = V_j\rho_j/\cos\theta_j$ is the seismic impedance, V_j the P-wave seismic velocity, ρ_j is bulk density and θ_j the reflection angle in media $j = 1, 2, 3$, related to each other by Snell's law.

As it can be seen from Equation 1 the layer P-wave reflectivity is complex, periodic and frequency dependent since $|k_2| = \frac{2\pi f}{V_2}$. The periodicity of R_{pp} is controlled by the layer thickness h, the layer velocity V_2 and the incidence angle θ_1.

The layer reflectivity modulus $|R_L|$ displays minima or *notchs* of (Liu and Schmitt, 2003)

$$|R_L(f,\theta_1)| = \left|\frac{Z_3 - Z_1}{Z_3 + Z_1}\right|, \tag{2}$$

when

$$k_{z2}h = \frac{2\pi h}{\lambda}\cos\theta_2 = m\pi, \quad m \in \mathbb{N}. \tag{3}$$

Of our particular interest is to rewrite the condition given by Equation 3 in term of the frequency. Since $\lambda = V_2/f$, the frequencies where the reflectivity notchs occur are given by

$$f_{\mathrm{n}}^m = m\,\frac{V_2}{2h\cos\theta_2}. \tag{4}$$

From the periodicity of the trigonometric functions, the *peak frequencies* where $|R_{pp}|$ shows maxima are given by

$$f_p^{m+1} = \left(\frac{1+2m}{2}\right)\frac{V_2}{2h\cos\theta_2}. \tag{5}$$

At normal incidence ($\theta_1 = 0$), the *first peak frequency* ($m = 0$) occurs at

$$f_p = \frac{V_2}{4h}. \tag{6}$$

In terms of the two-way time at normal incidence, $\Delta T = \frac{2h}{V_2}$, it follows that

$$f_p = \frac{1}{2\Delta T}, \tag{7}$$

what constitutes an useful relationship for the estimation of temporal thicknesses from peak frequencies (Williams and Chadwick (2012)). Figure 1 shows $|R_L(f,h)|$ at normal incidence for a fully saturated CO_2 layer of increasing h using the parameters of Table 1 and 2, as well as a Gassmann fluid substitution to calculate the seismic impact of the CO_2 saturation. The trends of the maxima are clearly visible.

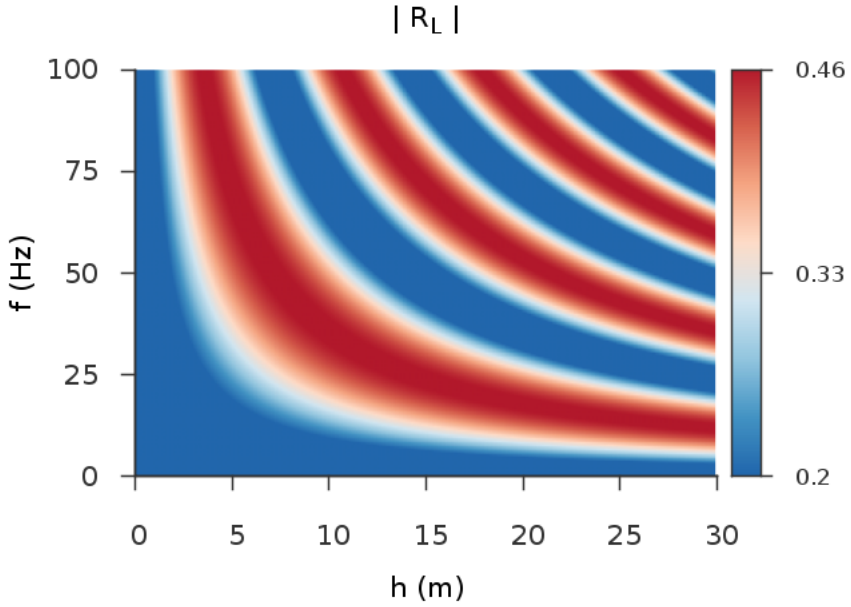

Figure 1: Modulus of the P-wave reflectivity $|R_L(f,h)|$ at normal incidence. The layer has $S_g = 100$ %.

3 SEISMIC ATTENUATION

After the injection, the CO_2 is most likely to be distributed irregularly at different scales within the in-situ brine, these spatial heterogeneities may give rise to *mesoscopic* seismic attenuation and dispersion phenomena. These effects are represented in this work by implementing a White's periodic model. Quintal et al. (2011) have shown that the mesoscopic model proposed

by White et al. (1975) gives a reasonable account for attenuation and velocity dispersion in finite media with random heterogeneities in fluid content. White's representative rock volume is composed of a fully CO_2 saturated lamina of thickness l_g and a fully saturated brine lamina of thickness l_b, being $l = l_g + l_b$ the length of White's sample (Figure 2). The CO_2 saturation of the lamination is then $\frac{l_g}{l_g+l_b}$. To account for the lack of specific knowledge on the in-situ saturation

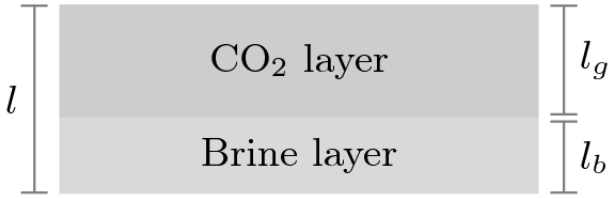

Figure 2: A sample of White's periodic model. l_g is the length of the CO_2 saturated lamina; the brine saturated lamina has length l_b.

of the CO_2 accumulation, for a given CO_2 saturation S_g between $[10\%, 90\%]$, we generate a sequence of N random saturations

$$S_j = S_g + \epsilon_j \Delta S \tag{8}$$

between $[S_g - \Delta S, S_g + \Delta S]$, where ϵ_j is a uniform random number between $[-1, 1]$ and $j = 1, \ldots, N$. In this way, the bulk density for each of White's samples is calculated by

$$\rho_j = \phi \left(S_j \rho_g + (1 - S_j) \rho_b \right) + (1 - \phi) \rho_m, \tag{9}$$

where ϕ is the sandstone porosity, ρ_g and ρ_b are the CO_2 and brine densities respectively listed in Table 2.

Since the CO_2 saturation is given in terms of $S_g = l_g/l$, according to the given S_j, we calculate the thicknesses of the CO_2 and brine laminae by $l_g = lS_j$ and $l_b = l - l_g$ respectively. In our tests, we consider $l = 0.5$ m and $\Delta S = 10\%$.

For every S_j we calculate, at each frequency f, the corresponding White's complex plane wave modulus $M_j(f, S_j)$ and average the results to obtain $\bar{M}(f, \bar{S}_g)$, where

$$\bar{S}_g = \frac{1}{N} \sum_{j=1}^{N} S_j, \tag{10}$$

is the overall CO_2 saturation. For the following tests we used $N = 100$. A histogram for the case $\bar{S}_g = 90\%$ is shown in Figure 3. Given the average plane-wave modulus, and average bulk density $\bar{\rho}(\bar{S}_g) = \frac{1}{N} \sum_{j=1}^{N} \rho_j$, following Carcione (2007), the complex P-wave velocity is

$$V(f, \bar{S}_g) = \sqrt{\frac{\bar{M}}{\bar{\rho}}}, \tag{11}$$

the P-wave phase velocity is calculated as

$$V^p(f, \bar{S}_g) = \left(Re \left\{ \frac{1}{V} \right\} \right)^{-1}, \tag{12}$$

and the quality factor is

$$Q(f, \bar{S}_g) = \frac{Re\{\bar{M}\}}{Im\{\bar{M}\}}. \tag{13}$$

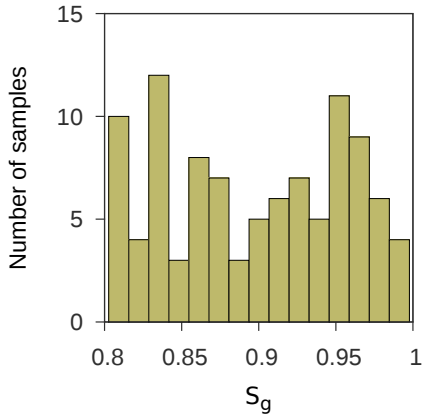

Figure 3: Histogram for the random CO_2 saturations S_j considered to make the overall value of $\bar{S}_g = 90\%$. 100 random saturations where considered between 80% and 100%.

4 CO_2 FLOW

The vertical distribution of the CO_2 saturation in the reservoir is modeled by the 1D Buckley-Leverett equation. Since for the considered reservoir the capillarity effects are not important (Gómez and Ravazzoli, 2012), the flow of the injected gas is modeled by means of the 1D buoyancy driven Buckley-Leverett equation without capillarity and constant porosity:

$$\phi \frac{\partial}{\partial t} S_g(t,z) + \frac{\partial}{\partial z} F(S_g,z) = 0, \tag{14}$$

where $S_g(t,z)$ is the CO_2 saturation, t is time, z is the vertical direction and ϕ porosity. $F(S_g,z)$ is the global flux function,

$$F(S_g,z) = \frac{1}{\mu_b} k_{rb} K(z) f(S_g)(\rho_b - \rho_g)g. \tag{15}$$

μ_b and k_{rb} are the viscosity and relative permeability of brine, K the absolute permeability, g the gravity field modulus, ρ_b and ρ_g the brine and CO_2 density respectively. $f(S_g)$ is the fractional flux function,

$$f(S_g) = \frac{k_{rg}}{k_{rg} + \frac{\mu_g}{\mu_b} k_{rb}}, \tag{16}$$

being k_{rg} and μ_g the viscosity and relative permeability of CO_2.

The relative permeabilities are computed by the Brooks-Corey expressions (Brooks and Corey, 1966),

$$\begin{aligned} k_{rb}(S_g) &= (1 - S_{eg})^{\frac{2+3\lambda}{\lambda}} \\ k_{rg}(S_g) &= S_{eg}^2 \left[1 - (1 - S_{eg})^{\frac{2+\lambda}{\lambda}}\right] \end{aligned} \tag{17}$$

where λ is the pore size distribution index and

$$S_{eg} = \frac{S_g - S_{rg}}{1 - S_{rg} - S_{rb}} \tag{18}$$

is the effective gas saturation. S_{rb} and S_{rg} denote the residual brine and CO_2 saturation respectively.

The initial condition taken is $S_g = 0$. At the base of the computational domain ($z = -20$ m) the saturation will be held at 0.28% for all t, this means that the CO_2 is assumed to be injected continually from the bottom of the computational domain. The value of 0.28% is close to the value that makes F a maximum; which is the highest saturation permitted to travel in the domain. The condition at the base of the domain implies then that the CO_2 will enter the target reservoir ($z = 0$ m) as a shock of nearly constant saturation.

To numerically implement the Buckley-Leverett law we use the conditionally stable finite-difference relaxation method proposed by Seaïd (2006). The main advantage of this method is the simplicity of the resulting scheme that accurately solves the Buckley-Leverett law in the presence of permeability discontinuities. This method has been written as a `FORTRAN90` subroutine and tested against the results of Hayek et al. (2009) and Seaïd (2006). The relaxation scheme parameters applied are analogous of those in Gómez and Ravazzoli (2012). We refer to this publication for more details on the derivation of the Buckley-Leverett equation and its implementation.

Lithology	V_p [m/s]	V_s [m/s]	ρ [kg/m^3]
Shale	2270	850	2100
Sandstone	2050	620	2050

Table 1: Seismic velocities and density of the Sleipner sandstone and shale at the 100% brine saturated pre-injection state, taken from Williams and Chadwick (2012).

5 SEISMIC REFLECTIVITY OF THE CO_2 FLOW

Once the vertical distribution of the carbon dioxide flux has been simulated, the reservoir's P-wave reflectivity response at normal incidence is obtained using a matrix reflectivity method for layered media. The matrix reflectivity method is an stable recursion that, starting from the bottom of the reservoir, adds one layer at a time and computes its reflectivity. Once the top of the reservoir is reached, the method gives the frequency and angle dependent complex reflection and transmission coefficients of compressional P and vertical shear waves SV. The heart of this algorithm is based solely on the continuity of particle displacements and stress at the interfaces between the successive layers that compose the reservoir (Pride et al., 2002).

At normal incidence, the reflectivity algorithm takes the simple scalar form (Mavko et al., 2011),

$$\hat{R}^{(k)} = R^{(k)} + \frac{T^{(k)} E^{(k)} \hat{R}^{(k+1)} E^{(k)}}{1 + R^{(k)} E^{(k)} \hat{R}^{(k+1)} E^{(k)}} T^{(k)} \tag{19}$$

$$\hat{T}^{(k)} = \frac{\hat{T}^{(k+1)} E^{(k)}}{1 + R^{(k)} E^{(k)} \hat{R}^{(k+1)} E^{(k)}} T^{(k)} \tag{20}$$

where $\hat{R}^{(k)}$ and $\hat{T}^{(k)}$ are the generalized reflection and transmission coefficients up to layer $k = 1, \ldots, n+1$, where n is the number of layers considered. The reflection and transmission coefficients for scaled displacements of each layer k are

$$R^{(k)} = \frac{\rho_{k-1} V_{k-1} - \rho_k V_k}{\rho_{k-1} V_{k-1} + \rho_k V_k}, \tag{21}$$

$$T^{(k)} = \frac{2\sqrt{\rho_{k-1} V_{k-1} \rho_k V_k}}{\rho_{k-1} V_{k-1} + \rho_k V_k}, \tag{22}$$

Property	Value	Units
Porosity of sand, ϕ	0.37	[]
Permeability of sand, K_1	1×10^{-12}	[m^2]
Permeability of shale, K_2	5×10^{-14}	[m^2]
Matrix bulk modulus of sand, K_m	36.9	[GPa]
Matrix bulk modulus of shale, K_m	22.72	[GPa]
Density of brine, ρ_b	1040.0	[kg/m^3]
Density of CO_2, ρ_g	690.0	[kg/m^3]
Viscosity of brine, μ_b	0.25×10^{-3}	[Pa s]
Viscosity of CO_2, μ_g	4.38×10^{-5}	[Pa s]
Bulk modulus of of brine, K_b	2.305	[GPa]
Bulk modulus of CO_2, K_g	0.088	[GPa]
Residual saturation of brine, S_{rb}	0.20	[ ]
Residual saturation of CO_2, S_{rg}	0.05	[ ]
Pore size distribution index, λ	2	[ ]

Table 2: Main parameters for the reservoir. Data has been collected from Audigane et al. (2007); Chadwick et al. (2004); Hayek et al. (2009); Mouche et al. (2010) and Williams and Chadwick (2012).

$E^k = \exp(2\pi i\, f\, h_k/V_k)$ is the phase shift operator and i the imaginary unit. V_k is the P-wave velocity, ρ_k the density and h_k the thickness of layer k. The recursion begins at the base of the layering by setting $R^{(n+1)} = \hat{R}^{(n+1)} = 0$ and $T^{(n+1)} = \hat{T}^{(n+1)} = 1$. From the algorithm we obtain the sequence:

$$\hat{R}^{(n+1)}\,,\ \hat{R}^{(n)}\,,\ \hat{R}^{(n-1)},\quad \ldots\quad ,\hat{R}^{(1)}; \tag{23}$$

being $R_{pp}(f) \equiv \hat{R}^{(1)}$ the generalized reflection coefficient of the layered medium. By means of the correspondence principle (Ben-Menahen and Singh, 1981) we can extend this algorithm for a layered medium with velocity dispersion and attenuation. This algorithm was also written in `FORTRAN90` and interacts with the saturation profile given by the Buckley-Leverett subroutine by means of a driver script written in `bash`.

6 PEAK FREQUENCY AND CO_2 SATURATION

The main parameters that characterize the modeled CO_2 accumulation, and have a substantial impact in the seismic reflectivity, are the layer thickness h and overall gas saturation $\bar{S}_g$. Some spectral attributes, such as spectral gradient (Sulistyoati et al., 2011) and average frequency (Barnes et al., 2004), can not individualize the layer thickness effects from the CO_2 saturation on the reflectivity. For this reason, we investigate in this section how independent is the thickness estimation through f_p from the CO_2 saturation of the accumulation. The reservoir considered in this section is a poroelastic medium that consists of a CO_2 saturated layer between two halfspaces (Figure 4). The upper halfspace (medium 1), represents the Nørdland shale caprock. The embedded layer of thickness h (medium 2), is a Utsira sandstone partially saturated by immiscible CO_2 and brine. The CO_2 is at a supercritical state, behaving as a low-viscosity fluid. The bottom halfspace of the model (medium 3), consists of a Utsira sandstone fully saturated with brine. Seismic velocities and densities for the shale caprock and the fully brine saturated sandstone are shown in Table 1 and the physical properties of the reservoir fluids are listed in Table 2. In Figure 5a we plot the amplitude of the normal-incidence reflection coefficient for an accumulation of $h = 30$ m. This frequency-dependent reflectivity exhibits the effects of velocity dispersion (Figure 5b) and attenuation (5c) due to wave-induced fluid flow. A lowering

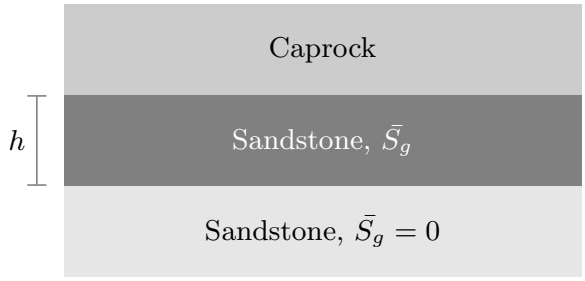

Figure 4: One CO_2-saturated layer between halfspaces to evaluate peak frequency in a CO_2 storage reservoir.

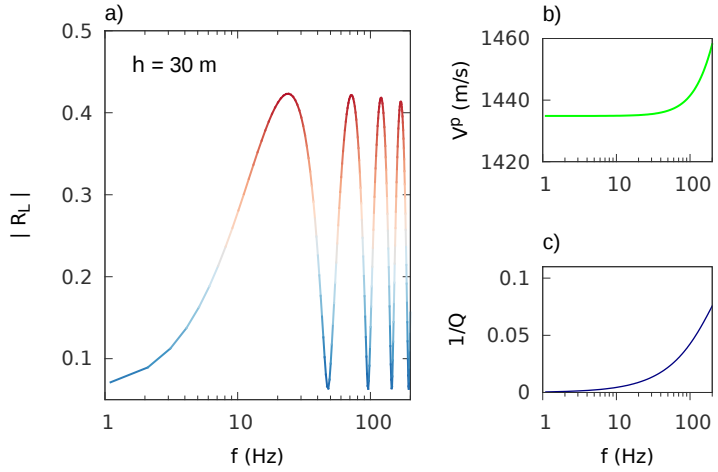

Figure 5: (a) Amplitude of the normal-incidence reflection coefficient of the layer, $|R_L|$, when layer thickness is $h = 30$ m. The CO_2 overall saturation is $\bar{S}_g = 50\%$. (b) P-wave phase velocity and (c) attenuation from White's model.

of $|R_L|$ amplitudes at high seismic frequencies, due to attenuation can be seen. At the zero frequency limit the layer reflectivity becomes the reflection coefficient between the halfspaces. The character of the normal-incidence reflectivity for White's model is shown in figure 6. As we can see, the trend of the peak frequency with layer thickness holds in the case of a non elastic medium. We assess next how robust is this relationship to changes in CO_2 saturation. Figure 7 shows the layer thickness versus peak frequency curve for overall CO_2 saturations between 10% and 90%. The case when $S_g = 0$ is not taken into account because it is the baseline case, where no CO_2 is yet present in the targeted reservoir. As we can see, the standard deviation in thickness estimation, given by the error bars, is acceptable. The sensitivity due to the varying overall CO_2 content starts to increases when h becomes small. For layers of $h < 4$ m, the standard deviation can be of over 20 Hz but the peak frequency is already beyond the seismic range $f < 120$ Hz. For $h > 4$ m the deviation is lower than 5 Hz. We conclude from this test that peak frequency is a viable estimator for layer thickness regardless of the overall CO_2 saturation content and the viscoelastic effects. This because the CO_2 saturation mainly modifies the $|R_L|$ amplitude but not the position of its notches and maxima.

In the next section we will show how a time-lapse computation of peak frequency can be used to trace the evolution of the CO_2 flow in a reservoir.

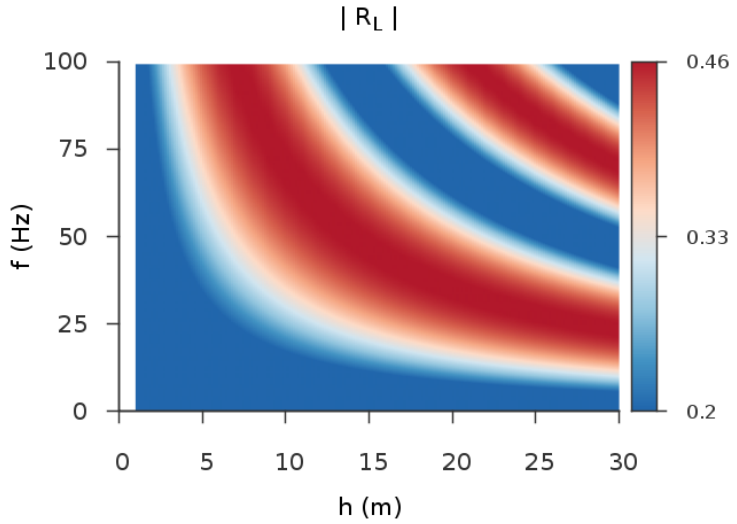

Figure 6: Modulus of the P-wave reflectivity $|R_L(f,h)|$ at normal incidence for White's model. The layer has $\bar{S}_g = 50\ \%$.

7 TIME-LAPSE PEAK FREQUENCY

Since the CO_2 accumulation thickness is given by the position of the CO_2-brine fluid contact, it is to expect that a time-lapse calculation of peak frequency should be able to track this fluid/fluid contact through time. Whether or not the CO_2 layer can be imaged explicitly by the seismic method, this could be used as a practical tool to interpret the CO_2 flow in a reservoir.

Based on Sleipner's topmost CO_2 accumulation, we consider a 20 m thick brine saturated Utsira sandstone overlain by a halfspace playing the role of the Nørdland shale caprock. At the base of the computational domain, 10 m below the target reservoir base, we consider a constant CO_2 saturation of 28 %. The CO_2 will enter the targeted sandstone reservoir at $z = 0$ as a saturation front. At the top of the domain we apply the condition of no CO_2 flow, $F = 0$, where F is the global flux function. As the reservoir is modeled as an assemblage of two lithological units, the highly permeable Utsira sandstone and the low-permeable shale caprock, the absolute permeability function takes the form

$$K(z) = \begin{cases} K_1, & \text{if } 0 \leqslant z \leqslant 20 \text{ m}; \\ K_2 < K_1, & \text{if } z > 20 \text{ m}. \end{cases} \tag{24}$$

We discretized the reservoir as a stack of n plane layers, of thickness h equal to the size of White's representative volume, i.e. $h = l$, with $l = 0.5$ m. The effect of the vertical distribution of CO_2 saturation in the P-wave velocity V_P for any layer in the reservoir is given by White's formula, using the methodology described in section 3. The only difference is that this time we use for each layer the CO_2 saturation $S_g(t,z)$ given directly by the Buckley-Leverett equation, instead of an overall time-independent mean $\bar{S}_g$. Once all the velocities and densities of the layered model are adjusted to the vertical saturation profile, the normal-incidence P-wave reflectivity R_{pp} for the stack of layers is obtained the reflectivity algorithm. The number of layers that comprises the reservoir varies from $n = 40$ for the sealed caprock case to $n = 60$ for the leaking caprock case.

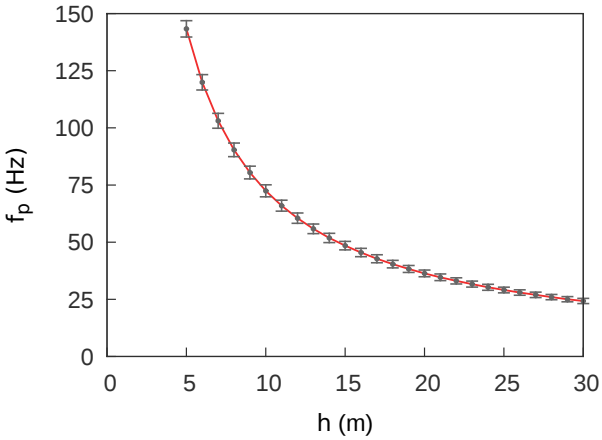

Figure 7: Average peak frequency $\bar{f}_p$ versus layer thickness h. Each point is an average over the CO_2 overall saturation $\bar{S}_g$ range between 10% to 90%. The vertical lines show the dispersion of the mean value, which increases as layer thickness becomes thinner.

In the following tests we consider two geologic storage situations, one where no upward migration into the caprock exists (*sealed caprock*), and another where leakage takes place into the shale (*unsealed caprock*). The parameters of the reservoir and fluids are given in Table 2. In the context of the CO_2 geological storage and monitoring it would be interesting to assess the difference between these two cases by means of a simple method as the peak frequency evolution proposed in this work. For the two reservoir models analyzed we calculate the curve of peak frequency in time. The results indicate that time-lapse peak frequency changes can describe the evolution of the CO_2 distribution and also evaluate reservoir integrity.

7.1 Sealed caprock

Figure 8 displays the vertical distribution of CO_2 and the associated seismic reflectivity at different times. The solution $S(t, z)$ is calculated using a time discretization of $t_s = 1$ day at height intervals of $\Delta z = 0.5$ m. Figures 8a to 8c show the evolution of the vertical CO_2 distribution at three different times. Figures 8d to 8f display the amplitude spectra of the reflectivities. Figure 8a shows the advancing CO_2 front at $\frac{t}{ts} = 4$. In Figure 8b, at $\frac{t}{ts} = 24$, the CO_2 has accumulated below the caprock, giving rise to a down-going front. Finally in 8c the vertical profile of CO_2 starts to become constant with height at $\frac{t}{ts} = 84$. As expected, the reflectivity at this point (Figure 8f) is rather independent of frequency. Figure 9 displays the time-lapse curve of the first peak frequency of $|R_{PP}|$. Three stages are clearly visible. (a) The CO_2 front is traveling upwards to reach the caprock. The peak frequency increases because the zone where $S_g = 0$ diminishes with time. The effect on the reflectivity is of a thinning fully saturated brine layer between a caprock and a CO_2 saturated sandstone. As the brine layer becomes thinner, the notches in the reflectivity move toward higher frequencies. This is the only stage where an increase in peak frequency with time is observed. (b) The CO_2 starts to accumulate under the caprock. As the CO_2 accumulation thickens, the peak frequency decreases in agreement with Equation 6. The transition between this stage and the previous one occurs when the ascending fluid/fluid contact reaches the base of the caprock. The curves in these stages are not exactly symmetrical due to the fact that in the previous stage there is a fully saturated brine zone whereas in this one CO_2 is present in all the reservoir. (c) After the fluid/fluid contact at the base of the accumulation leaves the target reservoir ($z < 0$), the CO_2 saturation will increase

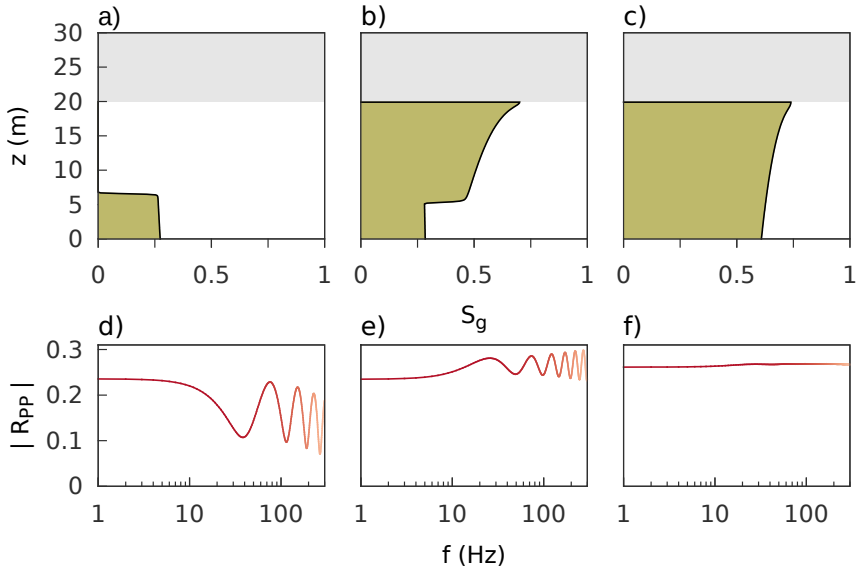

Figure 8: Vertical distribution of CO_2 and amplitude spectrum of the normal-incidence P-wave reflectivity R_{pp} at different times for a sealed caprock situation.

to reach the maximum value of $1 - S_{rb}$ (where S_{rb} is the residual brine saturation) and $S_g(t, z)$ will tend to a constant value for all z. We have seen in the first section that peak frequency is rather independent of CO_2 saturation, so the reflectivity will become rather constant with time. In this test, where no upward migration of CO_2 exists into the caprock, peak frequency becomes stable at a frequency related to a thickness of 20 m, as can be seen in the peak frequency versus thickness plot of Figure 6.

We have seen that when the CO_2 distribution stabilizes, the peak frequency becomes constant in time. In the next section, we will show that this time-lapse trend in peak frequency is modified if the CO_2 migrates vertically into the caprock. In this situation, the peak frequency attribute would also be able to identify an unfavorable leakage scenario.

7.2 Unsealed caprock

We consider now a situation where CO_2 has the potential to leak into the caprock and eventually originate a secondary accumulation. We consider for this purpose a model where the reservoir sandstone, of permeability K_1 is overlain by a 10 m Nørland shale with permeability K_2 given in Table 2. To account for the mesoscopic effects in the caprock due to the CO_2, we apply the White formulation to the shale, with a porosity of $\phi = 0.25$ from Carcione and Picotti (2006).

Figure 10 presents the CO_2 distribution and the P-wave reflectivity amplitude at three different stages. In Figures 10a and 10d, when $\frac{t}{ts} = 6$, the CO_2 front propagates upwards. In Figures 10b and 10e, at $\frac{t}{ts} = 19$, the reflected shock propagates downwards. In Figures 10c and 10f, when $\frac{t}{ts} = 94$, the distribution starts to become constant with high and a shock travels in the caprock. We show in Figure 11 how the time-lapse peak frequency curve varies when upward migration of CO_2 into the caprock occurs. As we can see, in stage (a) a CO_2 front goes towards the caprock, and in (b) a CO_2 accumulation develops. The differences with the sealed caprock (Figure 9) arises once the CO_2 reaches the caprock base at $z = 20$ m. At stage (c) the peak frequency displays a monotonic decrease in time due to the upward migration of CO_2 into the shale, as opposed to the constant trend of the sealed case. The length over time of the decreasing

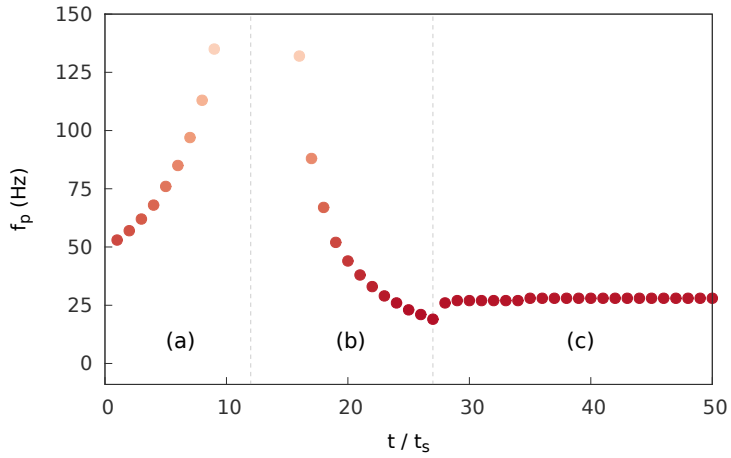

Figure 9: First peak frequency f_p over time t, for a perfectly sealed caprock reservoir. The time interval between the computation of each f_p in the plots is $t_s = 1$ day. A lighter red color is used indicate peak frequency points in the threshold of the seismic frequency range.

trend, is related to the value of the permeability on the shale. Lower caprock permeabilities will present longer peak frequency decrease trends than higher permeabilities. Eventually, this trend will reach frequencies very close to zero. At this moment, in stage (d), the first peak frequency adopts the trend of the 2nd peak frequency, which becomes stable once the CO_2 accumulates in the shale below $z = 30$ m. Similar to the sealed caprock case, the peak frequency will stabilize at stage (e), but this time at a higher frequency than a priori expected for a sandstone reservoir of 20 m.

The results indicate that a reservoir with CO_2 leakage presents, as main characteristics, a sustained decrease in the time-lapse peak frequency and a stabilization to a higher-than-expected frequency.

8 CONCLUSIONS

It has been shown in this paper that peak frequency is a robust spectral attribute for estimating layer thickness in a CO_2 storage aquifer. We have seen that its sensitivity to CO_2 saturation does not affect considerably the character of the attribute. We have also shown that a time-lapse computation of this attribute, has the potential to delineate and characterize the vertical distribution of the injected CO_2. In this way, peak frequency signatures for the stages when the CO_2 forms an up-going front, a growing accumulation or an upward leakage into a caprock can be identified. The peak frequency analysis presented in this work is not limited to saturation profiles derived from the Buckley-Leverett equation and can be extended to arbitrary saturation profiles.

It is worthwhile to point out that the analysis of the peak frequency attribute with real seismic data would require: (i) a high-resolution time-lapse seismic data to reach the peak frequencies related to thin layers; (ii) spectral balancing to remove the effect of the seismic source on the amplitude spectra of the seismic traces; (iii) isolation of a window containing the seismic reflections associated to CO_2-brine contacts; (iv) determination of peak frequencies and their time-lapse variations through an appropriate time-frequency decomposition on the selected seismic window.

A 2D distribution of the CO_2 in the Sleipner reservoir should not display, due to the high homogeneity of the rocks, much different vertical profiles than the considered in this work.

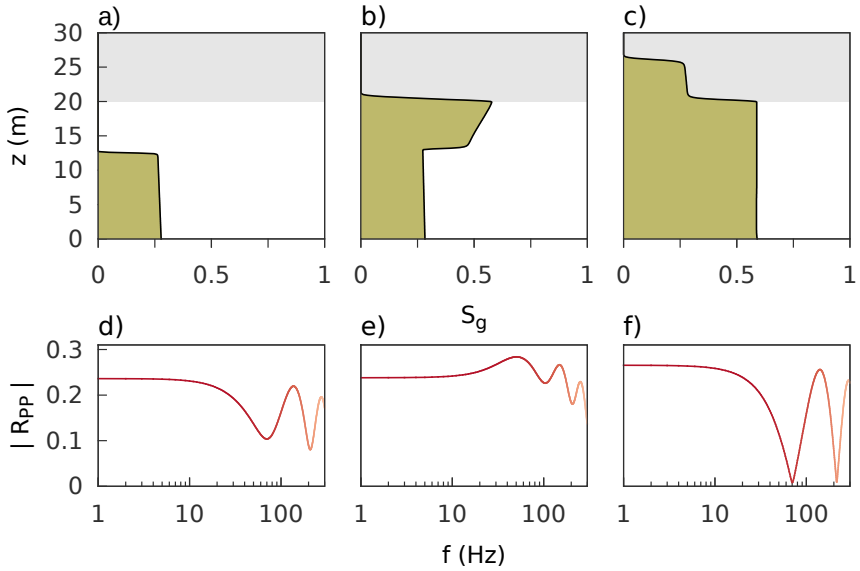

Figure 10: Vertical distribution of CO_2 and amplitude spectrum of the normal-incidence P-wave reflectivity R_{pp} at different times for a leaking caprock situation.

This means that the results and conclusions will hold in that situation. The 1D representation developed in this manuscript provides then of a basis for generalizations to higher dimensions.

We expect that the theoretical time-lapse results of this work may contribute as a practical tool to guide in the seismic interpretation of field data.

9 ACKNOWLEDGMENTS

This work was partially supported by CONICET (Argentina) PIP 112-200801-00952 and Programa de Incentivos, Universidad Nacional de La Plata (UNLP).

REFERENCES

Audigane P., Gaus I., Czernichowski-Lauriol I., Pruess K., and Xu T. Two-dimensional reactive transport modelling of CO_2 injection in a saline aquifer at the Sleipner site, north sea. *American Journal of Science*, 307:974–1008, 2007.

Barnes A.E., Fink L., and Laughlin K. Improving frequency domain thin bed analysis. *SEG Technical Program Expanded Abstracts 2004*, pages 1929–1932, 2004. doi:10.1190/1.1851175.

Ben-Menahen A. and Singh S.J. *Seismic Waves and Sources*. Springer-Verlag, first edition, 1981. ISBN 0-387-90506-6.

Brooks R.H. and Corey A.T. Properties of porous media affecting fluid flow. *Journal of the Irrigation and Drainage Divison of the American Society of Civil Engineers*, 92(IR2):61–88, 1966.

Carcione J.M. *Wave Fields in Real Media. Theory and Numerical Simulation of Wave Propagation in Anisotropic, Anelastic, Porous and Electromagnetic Media*. Elsevier, Amsterdam, 2 edition, 2007.

Carcione J.M. and Picotti S. P-wave seismic attenuation by slow-wave diffusion: Effects of inhomogeneous rock properties. *Geophysics*, 71(3):O1–O8, 2006. doi:10.1190/1.2194512.

Chadwick R.A., Arts R., and Eiken O. 4D seismic quantification of a growing CO_2 plume at Sleipner, North Sea. *Petroleum Geology: North-West Europe and Global Perspectives-*

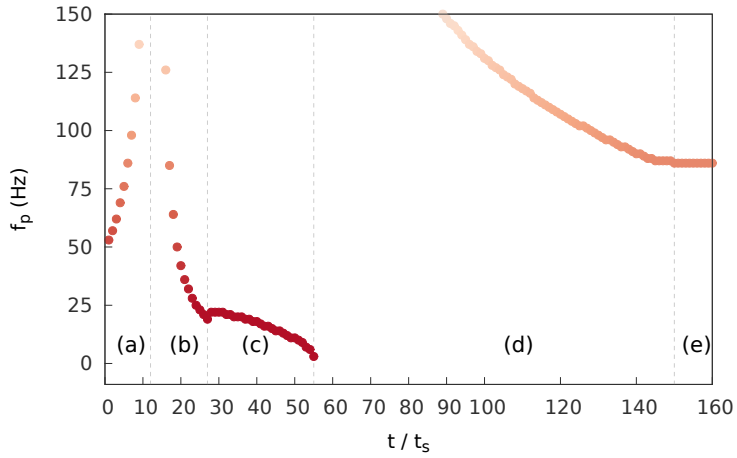

Figure 11: Peak frequency f_p over time t, for a leaking caprock reservoir. First peak frequency is shown. The time interval between the computation of each f_p in the plots is $t_s = 1$ day.

Proceedings of the 6th Petroleum Geology Conference, pages 1385–1399, 2005.

Chadwick R.A., Zweigel P., Gregersen U., Kirby G.A., Holloway S., and Johannessen P.N. Geological reservoir characterization of a CO_2 storage site: The Utsira Sand, Sleipner, northern North Sea. *Energy*, 29:1371–1381, 2004.

Gómez J.L. and Ravazzoli C.L. Seismic reflectivity of a carbon dioxide flux. *Mecánica Computacional*, 31:631–649, 2012.

Hayek M., Mouche E., and Mügler C. Modeling vertical stratification of CO_2 injected into a deep layered aquifer. *Advances in Water Resources*, 32:450–462, 2009.

Liu Y. and Schmitt D. Amplitude and avo responses of a single thin bed. *GEOPHYSICS*, 68(4):1161–1168, 2003. doi:10.1190/1.1598108.

Marfurt K. and Kirlin R. Narrow-band spectral analysis and thin-bed tuning. *Geophysics*, 66(4):1274–1283, 2001. doi:10.1190/1.1487075.

Mavko G., Mukerji T., and Dvorkin J. *The Rock Physics Handbook: Tools for Seismic Analysis of Porous Media*. Cambridge University Press, 2nd. edition, 2011.

Mouche E., Hayek M., and Mügler C. Upscaling of CO_2 vertical migration through a period layered porous medium: The capillary-free and capillary-dominant cases. *Advances in Water Resources*, 33:1164–1175, 2010.

Pride S., Tromeur E., and G. Berryman J. Biot slow-wave effects in stratified rock. *Geophysics*, 67(1):271–281, 2002. doi:10.1190/1.1451799.

Puryear C. and Castagna J. Layer-thickness determination and stratigraphic interpretation using spectral inversion: Theory and application. *Geophysics*, 73(2):R37–R48, 2008. doi:10.1190/1.2838274.

Quintal B., Steeb H., Freher M., and Schmalholz S.M. Quasi-static finite element modeling of seismic attenuation and dispersion due to wave–induced fluid flow in poroelastic media. *J. Geophys. Res.*, 116(B01201):n/a–n/a, 2011. doi:10.1029/2010JB007475.

Seaïd M. Stable numerical methods for conservation laws with discontinuous flux function. *Applied Mathematics and Computation*, 175:383–400, 2006.

Sulistyoati T.W.A., Novitasari L., and Winardhi S. Thickness estimation using gradient of spectral amplitude from spectral decomposition. *SEG Technical Program Expanded Abstracts 2011*, pages 1923–1927, 2011. doi:10.1190/1.3627583.

White J.E., Mikhaylova N.G., and Lyakhovitskiy F.M. Low-frequency seismic waves in fluid-

saturated layered rocks. *Izv. Acad. Sci. USSR Phys. Solid Earth, Engl. Transl.*, 11:654–659, 1975.

Williams G. and Chadwick A. Quantitative seismic analysis of a thin layer of CO_2 in the Sleipner injection plume. *Geophysics*, 77(6):R245–R256, 2012. doi:10.1190/geo2011-0449.1.